Schweizerischer Erdbebendienst
Service Sismologique Suisse
Servizio Sismico Svizzero
Servizi da Terratrembels Svizzer

ETH
Eidgenössische Technische Hochschule Zürich
Swiss Federal Institute of Technology Zurich

Altdorf - Spital (SALTS)

SITE CHARACTERIZATION REPORT

Clotaire MICHEL, Daniel ROTEN, Carlo CAUZZI

Valerio POGGI, Jan BURJANEK, Donat FÄH

Sonneggstrasse 5 CH-8092 Zürich Switzerland; E-mail: clotaire.michel@sed.ethz.ch

Last modified : November 5, 2013

Abstract

Ambient vibration array measurements were performed in the Reuss basin in Altdorf. The station SALTS of the Swiss Strong Motion Network located at the Altdorf hospital site was newly installed in 2012. In order to characterize the velocity profile under the station, array measurements with a $240\,\mathrm{m}$ aperture were performed. The H/V survey and polarization analysis showed that the Reuss basin has a fundamental frequency around $1.2\,\mathrm{Hz}$ at the station site. This resonance may however be related to a 2D/3D behaviour of the alluvial fan. The array measurements presented in this study were successful in deriving a velocity model below the SALTS station. We found a gradient-type velocity profile from $300 - 400\,\mathrm{m/s}$ at the surface increasing up to $800\,\mathrm{m/s}$ between 50 and $90\,\mathrm{m}$ and up to $1500\,\mathrm{m/s}$ at $300\,\mathrm{m}$. The interface between sediment and bedrock is represented by a peak at $1.2\,\mathrm{Hz}$ in the ellipticity. We derived a bedrock depth of $320\,\mathrm{m}$, which is consistent with geophysical and geomorpological data. The velocity in the bedrock is poorly constrained. $V_{s,30}$ is found to be close to $470\,\mathrm{m/s}$, which corresponds to ground type B in Eurocode 8 and SIA261 design codes. The theoretical SH transfer function and impedance contrast of the quarter-wavelength velocity computed from the inverted profiles show limited amplification at the resonance frequencies. Recordings on the new station will allow to validate these simple models.

Contents

1 Introduction

The station SALTS (Altdorf Spital) is part of the Swiss Strong Motion Network (SSMNet) in Central Switzerland. SALTS has been installed in the framework of the SSMNet Renewal project in 2012, as a new site. This project includes also the site characterization. Passive array measurements have been selected as a standard tool to investigate these sites. Such a measurement campaign was carried out on 28th August 2012 in the hospital area in Altdorf (Fig. 1), in order to characterize the soil column under SALTS station. The city was heavily damaged during a series of events in 1774 (I_0 =VIII) but the archives were lost so that no detailed assessment of the damage exist that could have help understanding the seismic risk in this area [Fritsche, 2008]. According to the geological map and Nitsche et al. [2002], the station SALTS is located on the loose alluvia of Lake Lucerne, Reuss river and the alluvial fan of surrounding slopes. Moreover, single station measurements in several points were already available in the city [Bühler, 2006]. This report presents the measurement setup, the results of the H/V analysis and of the array processing of the surface waves (dispersion curves). Then, an inversion of these results for velocity profiles is performed. Standard parameters are derived to evaluate the amplification at this site.

Canton	City	Location	Station code	Site type	Slope
Uri	Altdorf	Spital	SALTS	Deep sediments	Flat

Table 1: Main characteristics of the study-site.

Figure 1: Picture of the site.

2 Experiment description

2.1 Ambient Vibrations

The ground surface is permanently subjected to ambient vibrations due to:

- natural sources (ocean and large-scale atmospheric phenomena) below $1\,\mathrm{Hz}$,
- local meteorological conditions (wind and rain) at frequencies around $1\,\mathrm{Hz}$,
- human activities (industrial machines, traffic…) at frequencies above $1\,\mathrm{Hz}$ [Bonnefoy-Claudet et al., 2006].

The objective of the measurements is to record these ambient vibrations and to use their propagation properties to infer the underground structure. First, the polarization of the recorded waves (H/V ratio) is used to derive the resonance frequencies of the soil column. Second, the arrival time delays at many different stations are used to derive the velocity of surface waves at different frequencies (dispersion). The information (H/V, dispersion curves) is then used to derive the properties of the soil column using an inversion process.

2.2 Equipment

For the array measurements, 12 Quanterra Q330 dataloggers named NR01 to NR12 and 14 Lennartz 3C 5 s seismometers were available (see Tab. 2). Each datalogger can record on 2 ports A (channels EH1, EH2, EH3 for Z, N, E directions) and B (channels EH4, EH5, EH6 for Z, N, E directions). Time synchronization was ensured by GPS. The sensors were placed on a metal tripod in a $20\,\mathrm{cm}$ deep hole, when possible, for better coupling with the ground.

Digitizer	**Model**	**Number**	**Resolution**
	Quanterra Q330	12	$24\,\mathrm{bits}$
Sensor type	**Model**	**Number**	**Cut-off frequency**
Velocimeter	Lennartz 3C	14	$0.2\,\mathrm{Hz}$

Table 2: Equipment used.

2.3 Geometry of the arrays

Two array configurations were used, for a total of 4 rings of 10, 25, 50 and $120\,\mathrm{m}$ radius around a central station. The first configuration includes the 3 inner rings with 14 sensors; the second configuration includes the 2 outer rings (plus the inner ring and the central station) with 14 sensors. The largest ring is not centered as the others due to field constraints. The minimum inter-station distance and the aperture are therefore 10 and $100\,\mathrm{m}$ and 10 and $240\,\mathrm{m}$, respectively. The experimental setup is displayed in Fig. 2. The final usable datasets are detailed in section 3.2.

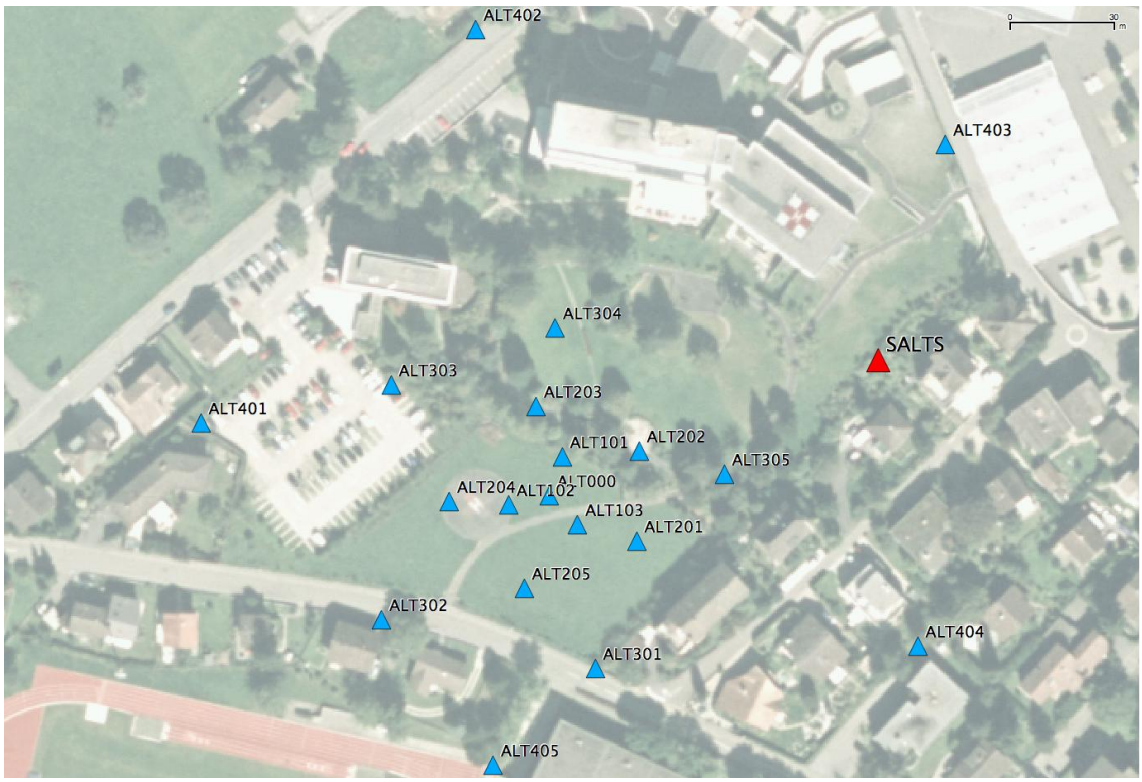

Figure 2: Geometry of the arrays.

2.4 Positioning of the stations

The sensor coordinates were measured using a differential GPS device (Leica Viva), including only a rover station and using the Real Time Kinematic technique provided by Swisstopo. It allows an absolute positioning with an accuracy of about $5\,\mathrm{cm}$ on the Swissgrid. However, for points ALT303, ALT305, ALT401 and ALT405 the precision was only 22, 25, 16 and $22\,\mathrm{cm}$, respectively, due to the presence of trees or metallic poles.

3 Data quality

3.1 Usable data

The largest time windows were extracted, for which all the sensors of the array were in position and the GPS synchronization was ensured. Differential GPS measurements were typically not performed during the data acquisition. Points ALT301, ALT302 and ALT402, located along a road show extremely large noise levels at low frequencies probably due to the air flow acting on the sensors when cars are passing by.

The North alignment of the sensors was double-checked by maximizing the correlation with the central station at low frequencies [Poggi et al., 2012b]. Deviations lower than $6\,^\circ$ were found for all points except for ALT402 ($16\,^\circ$) and ALT403 ($13\,^\circ$). Original and rotated datasets are available for the 3C array analysis.

The characteristics of the datasets are detailed in Tab. 3.

3.2 Data processing

The data were first converted to SAC format including in the header the sensor coordinates (CH1903 system), the recording component and a name related to the position. The name is made of 3 letters characterizing the location (ALT here), 1 digit for the ring and 2 more digits for the number in the ring. Recordings were not corrected for the instrument response.

Dataset	Starting Date	Time	Length	F_s	Min. inter-distance	Aperture	# of points
1	2012/08/28	8:57	122 min	200 Hz	10 m	100 m	14
2	2012/08/28	11:34	124 min	200 Hz	10 m	240 m	14

Table 3: Usable datasets.

4 H/V processing

4.1 Processing method and parameters

In order to process the H/V spectral ratios, several codes and methods were used. The classical H/V method was applied using the Geopsy `http://www.geopsy.org` software. In this method, the ratios of the smoothed Fourier Transform of selected time windows are averaged. Tukey windows (cosine taper of 5% width) of $100\,\mathrm{s}$ long overlapping by 50% were selected. Konno and Ohmachi [1998] smoothing procedure with b=60 was used. The classical H/V method of Fäh et al. [2001] was also applied.

Moreover, the time-frequency analysis method [Fäh et al., 2009] was used to estimate the ellipticity function more accurately using the Matlab code of V. Poggi. In this method, the time-frequency analysis using the Wavelet transform is computed for each component. For each frequency, the maxima over time (10 per minute with at least $0.1\,\mathrm{s}$ between each) in the TFA are determined. The Horizontal to Vertical ratio of amplitudes for each maxima is then computed and statistical properties for each frequency are derived. Cosine wavelet with parameter 9 was used. The mean of the distribution for each frequency is stored. For the sake of comparison, the time-frequency analysis of Fäh et al. [2001], based on the spectrogram, was also used, as well as the wavelet-based TFA coded in Geopsy.

The ellipticity extraction using the Capon analysis [Poggi and Fäh, 2010] on the array measurement was also performed (see section 5).

Method	Freq. band	Win. length	Anti-trig.	Overlap	Smoothing
Standard H/V Geopsy	$0.2-20\,\mathrm{Hz}$	$100\,\mathrm{s}$	No	50%	K&O 60
Standard H/V D. Fäh	$0.2-20\,\mathrm{Hz}$	$30\,\mathrm{s}$	No	75%	-
H/V TFA Geopsy	$0.2-20\,\mathrm{Hz}$	Morlet m=8 fi=1	No	-	-
H/V TFA D. Fäh	$0.2-20\,\mathrm{Hz}$	Specgram	No	-	-
H/V TFA V. Poggi	$0.2-20\,\mathrm{Hz}$	Cosine wpar=9	No	-	No

Table 4: Methods and parameters used for the H/V processing.

4.2 H/V results on the array data

H/V curves are similar for all the recordings acquired for the array processing (Fig. 3) showing there is no lateral variation in the array (Fig. 4). Moreover, all the methods to compute H/V ratios are compared on Fig. 5, where the classical methods were divided by $\sqrt{2}$ to correct for Love wave influence [Fäh et al., 2001]. The matching is good concerning the right flanks, but the amplitude and the peak are scattered. The 3C FK analysis provides the same results but is not able to explore the part related to the fundamental frequency due to the too small array aperture compared to the basin depth. The peak is relatively clear at $1.2\,\mathrm{Hz}$, with a peak amplitude around 3.

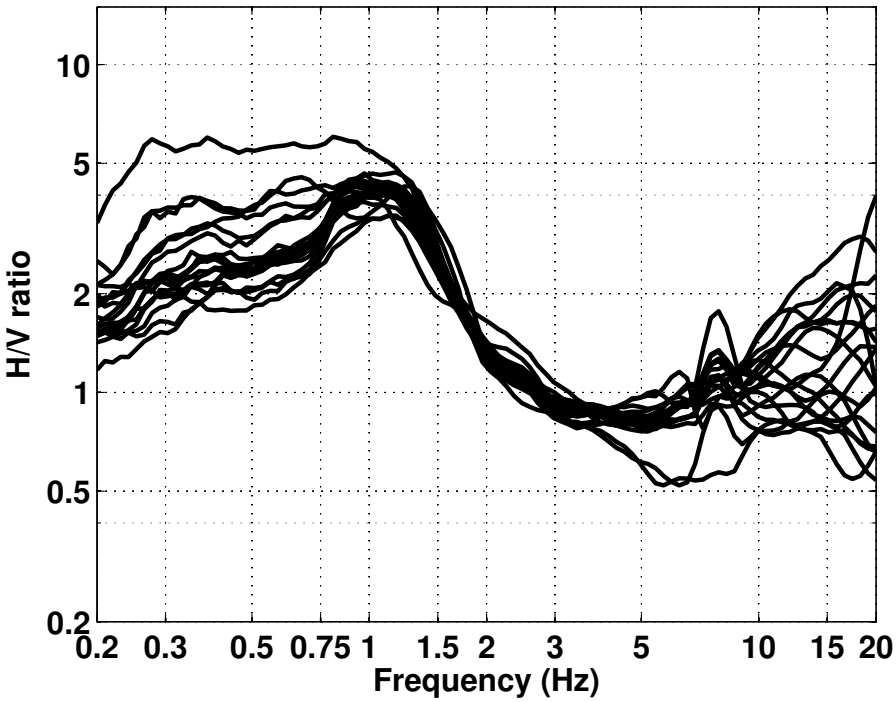

Figure 3: H/V spectral ratios of the array recordings (time-frequency analysis code V. Poggi).

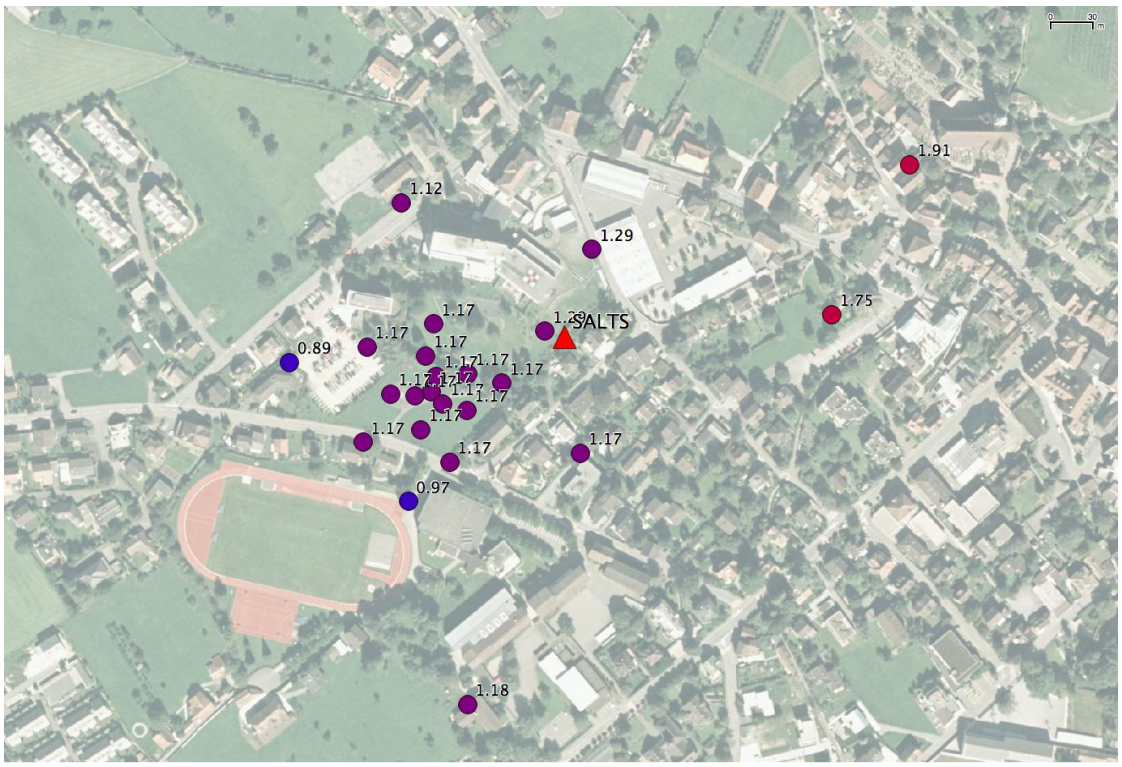

Figure 4: Fundamental frequencies in the array.

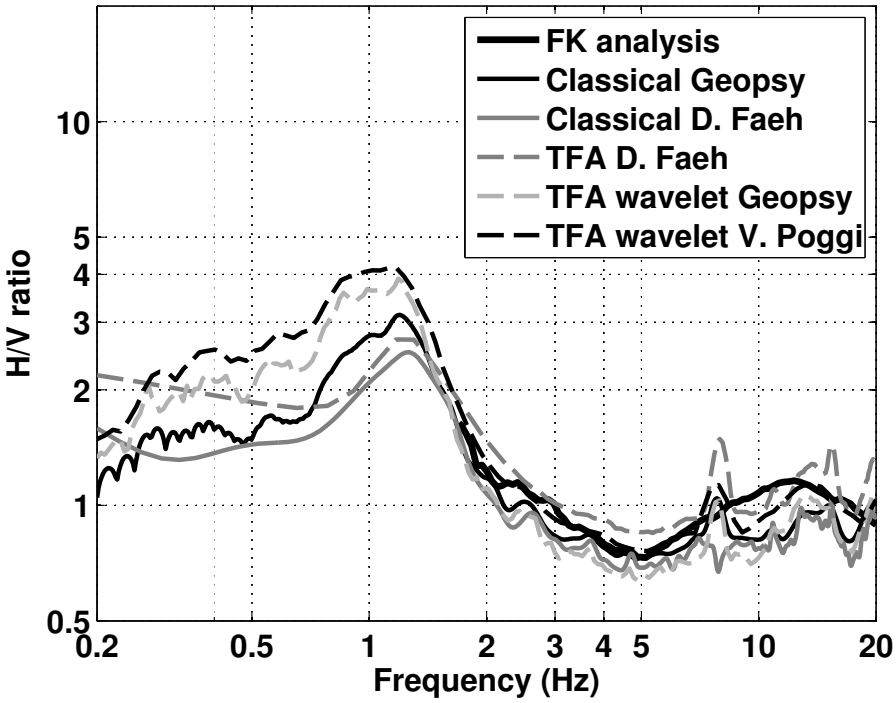

Figure 5: H/V spectral ratios for point ALT101 using the different codes. Classical methods were divided by $\sqrt{2}$.

4.3 H/V single point measurements in Altdorf

Other points from the SED database, performed by S. Fritsche and published in the semester work of Bühler [2006], as well as results from long-term test stations, are available for the area (Fig. 6). They show the increase of the fundamental frequency towards the basin edge (city-centre - Northeast) up to $3.4\,\mathrm{Hz}$ and a decrease in the direction of the valley-centre (Southwest) down to $0.5\,\mathrm{Hz}$. These variations are relatively smooth, which supports our interpretation that the alluvial fan below Altdorf is consistent with the behaviour expected for a 1D site. Moreover, it shows that the SSMNet stations is representative of the city-centre.

4.4 Polarization analysis

Considering the geometry of the Reuss valley, a polarization analysis using the code of Burjánek et al. [2010] was performed in order to determine if the observed H/V peak is related to 2D resonance. The results show the motion is horizontally polarized (H/V peak) and a preferred polarization at this frequency is visible in the ENE-WSW direction, i.e. in the direction of the alluvial fan (Fig. 7). However, this polarization is not very pronounced but may correspond to a 2D/3D behaviour of the alluvial fan. This is assumed as irrelevant for the rest of this report, but should be kept in mind for future research.

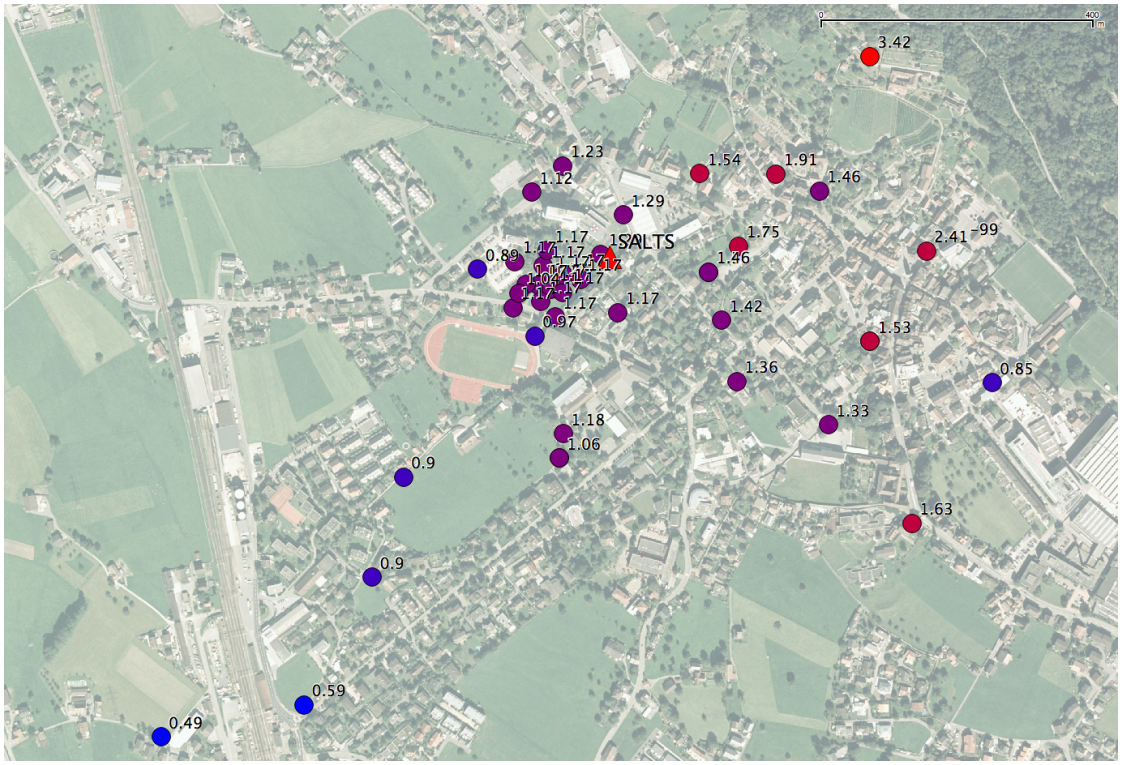

Figure 6: Fundamental frequencies in the city of Altdorf.

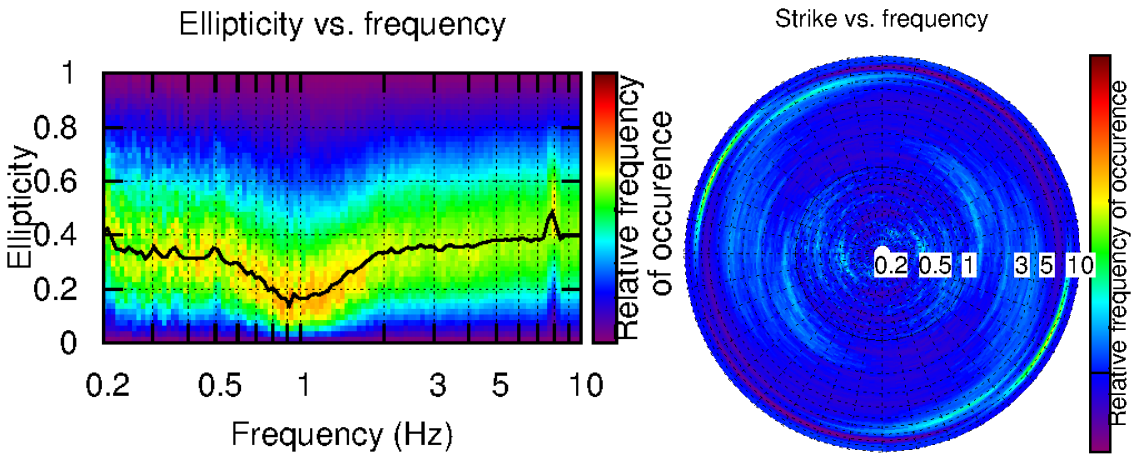

Figure 7: Polarization analysis at point ALT101. Left: Ellipticity (A trough in the ellipticity corresponds to horizontally polarized motion). Right: Strike of the polarization.

5 Array processing

5.1 Processing methods and parameters

The vertical components of the arrays were processed using the High-resolution FK analysis [Capon, 1969] using the Geopsy `http://www.geopsy.org` software. Better results were obtained using large time windows (300T, where T stands for period). The FK distributions were concatenated.

Moreover, a 3C array analysis [Fäh et al., 2008] was also performed using the array_tool_3C software [Poggi and Fäh, 2010]. The results of computations of both datasets were merged to estimate the dispersion curves. It allows to derive Rayleigh and Love fundamental modes.

Method	Set	Freq. band	Win. length	Anti-trig.	Overlap	Grid step	Grid size	# max.
HRFK 1C	1	$1-20\,\mathrm{Hz}$	$300T$	No	50%	0.001	0.5	5
HRFK 1C	2	$1-20\,\mathrm{Hz}$	$300T$	No	50%	0.001	0.5	5
HRFK 3C	1	$1-20\,\mathrm{Hz}$	Wav. 10	No	50%	200	3000	5
			Tap. 0.2			m/s	m/s	
HRFK 3C	2	$1-20\,\mathrm{Hz}$	Wav. 10	No	50%	200	3000	5
			Tap. 0.2			m/s	m/s	

Table 5: Methods and parameters used for the array processing.

5.2 Obtained dispersion curves

The fundamental mode (Rayleigh) in the 1C FK analysis could be picked between 1.8 and $17\,\mathrm{Hz}$ and the first higher mode between 6 and $20\,\mathrm{Hz}$ (Fig. 8) including their standard deviation. The phase velocities of the fundamental mode are ranging from $1900\,\mathrm{m/s}$ at $1.8\,\mathrm{Hz}$ down to $400\,\mathrm{m/s}$ at $17\,\mathrm{Hz}$.

Using the 3C analysis, both Rayleigh and Love modes can be picked (Fig. 8). The fundamental and first higher Rayleigh modes show no difference compared to the 1C analysis (Fig. 10). The phase velocity of the fundamental mode of the love wave identified from dataset 1 is different to the velocity identified from dataset 2 at low frequency (Fig. 9). The picked phase velocity of the Love wave identified from dataset 1 is very close to the identified Rayleigh wave phase velocity. It is not clear whether it is due to picking outside the array limit for dataset 1, a ghost of Rayleigh mode on dataset 1 or lateral variability within the array.

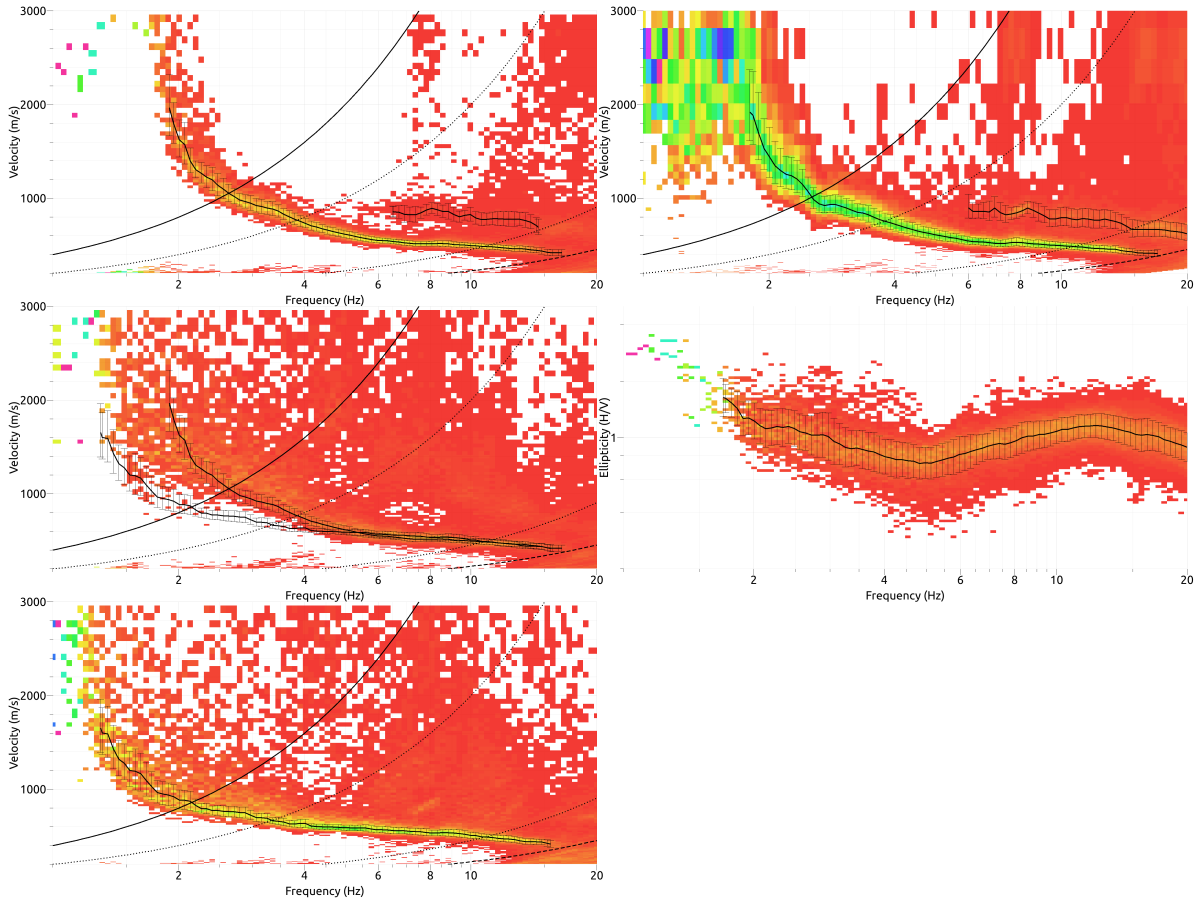

Figure 8: Dispersion curves and ellipticity obtained from the 1C (top right) and 3C array analysis (left and centre-right). Top: Vertical - Centre: Radial - Bottom: Transverse component

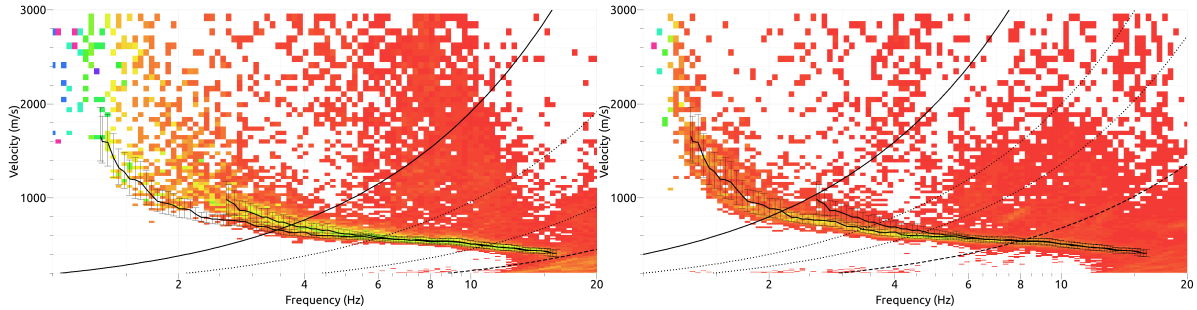

Figure 9: Love fundamental dispersion curves obtained from the 3C array analysis: datasets 1 (left) and 2 (right).

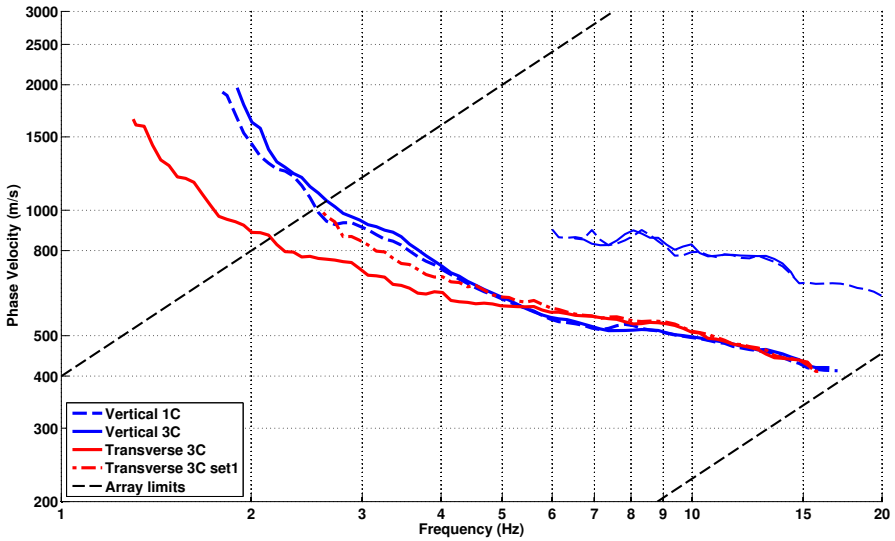

Figure 10: Picked dispersion curves from 1C and 3C analyses.

6 Inversion and interpretation

6.1 Inversion

For the inversion, the Love and Rayleigh fundamental modes (3C analysis) dispersion curves between 2 and $16\,\mathrm{Hz}$, the first Rayleigh higher mode (1C analysis), the right flank of the ellipticity peak (TFA code Poggi) and the peak $1.2\,\mathrm{Hz}$ at were used as simultaneous targets without standard deviation to avoid different weighting. A weight of 0.3 was assigned to the ellipticity curve, and 0.2 to the peak. All curves were resampled using 50 points between 0.8 and $21\,\mathrm{Hz}$ in log scale. It should be noticed that fundamental Love and Rayleigh dispersion curves below the array limit were found to be strongly biased and were not used in the inversion.

The inversion was performed using the Improved Neighborhood Algorithm (NA) [Wathelet, 2008] implemented in the Dinver software. In this algorithm, the tuning parameters are the following: Ns_0 is the number of starting models, randomly distributed in the parameter space, Nr is the the number of best cells considered around these Ns_0 models, Ns is the number of new cells generated in the neighborhood of the Nr cells (Ns/Nr per cell) and It_{max} is the number of iteration of this process. The process ends with $Ns_0 + Nr * \frac{Ns}{Nr} * It_{max}$ models. The used parameters are detailed in Tab. 6.

It_{max}	Ns_0	Ns	Nr
500	10000	100	100

Table 6: Tuning parameters of Neighborhood Algorithm.

During the inversion process, low velocity zones were not allowed. The Poisson ratio was inverted in each layer in the range 0.2-0.4, up to 0.47 in the upper layers, below the hypothetic ground water table and the density was supposed equal to $2000\,\mathrm{kg/m^3}$ except for the deepest layers ($2500\,\mathrm{kg/m^3}$). Inversions with free layer depths as well as fixed layer depths were performed. 5 layers are enough to explain most of the targets (dispersion and ellipticity), but more layers are used to smooth the obtained results and better explore the parameter space. 5 independent runs of 5 different parametrization schemes (5 and 7 layers over a half space and 10, 12 and 13 layers with fixed depth) were performed. For further elaborations, the best models of these 25 runs were selected (Fig. 13).

The inverted models are characterized by a gradually increasing shear-wave velocity: Vs is between 300 and $400\,\mathrm{m/s}$ at the surface and reaches $1500\,\mathrm{m/s}$ at a depth of 300 m. Between 50 and $90\,\mathrm{m}$ depth, the shear-wave velocity increases rapidly from 400 to $800\,\mathrm{m/s}$. The bedrock depth, generating the ellipticity peak at $1.2\,\mathrm{Hz}$, is poorly constrained but found at $320\,\mathrm{m}$ by the free layer depth inversions. The fixed-layer depth inversion show a stronger gradient below this depth. The velocity in the bedrock is poorly constrained, but found around $2700\,\mathrm{m/s}$.

When compared to the target curves (Fig. 11), all dispersion curves are well reproduced. The ellipticity is also well reproduced, but the constraints on the deepest layers are anyway weak.

Nitsche et al. [2002] published the results of a $300\,\mathrm{m}$ deep borehole and a seismic survey in the Reuss valley close to Altdorf for the central part of the valley. The borehole is located

closer to the surveyed area in Altdorf than the seismic survey. They recognized horizontal layers across the valley. The units from the borehole are a first layer of gravels and sand down to $127\,\mathrm{m}$, a layer of sands and silts with rare gravels down to $175\,\mathrm{m}$ and a layer of sands and silts down to $298\,\mathrm{m}$ (coarser down to finer material). At this depth, a major change in lithology occurs from fine sand to lacustrine clay. These lacustrine sediments are assumed to be present down to the bedrock. They also give the bedrock shape and depth but the surveyed part does not reach the edge of the valley where the SSMNet station is installed. In terms of velocity, it is not surprising that this series of sediments do not show sharp velocity contrasts but a velocity gradient as found in the inversion.

Assuming the topographic slope of the rock surrounding the valley remains constant below the sediments ($38\,^\circ$ from the Swisstopo map), the sediment thickness is found to be around $325\,\mathrm{m}$ below the SALTS station. It is coherent with what was found here using the free depth inversion ($320\,\mathrm{m}$). Moreover, extrapolating the bedrock depth from the Nitsche et al. [2002] profile gives $300\,\mathrm{m}$ for the weathered bedrock and $320\,\mathrm{m}$ for the hard bedrock.

It can be noticed that the models with the deepest layers showing a gradient instead of a sharp contrast at the bedrock depth fit better the Rayleigh dispersion curve. It is therefore not excluded that the velocity profile in the bedrock is complex, but the proposed data cannot definitely conclude on this point.

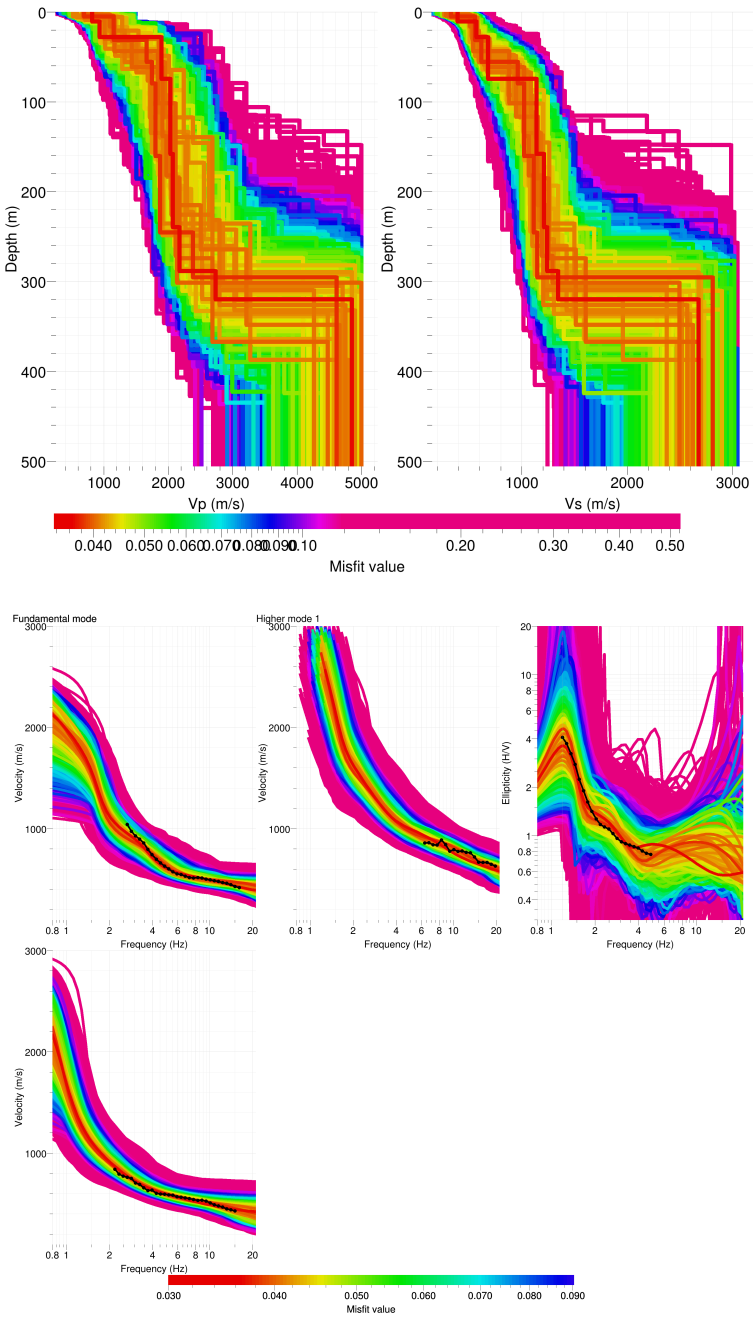

Figure 11: Inverted ground profiles in terms of V_p and V_s (top) and comparison between inverted models and measured Rayleigh and Love modes and corresponding ellipticity, free layer depth strategy.

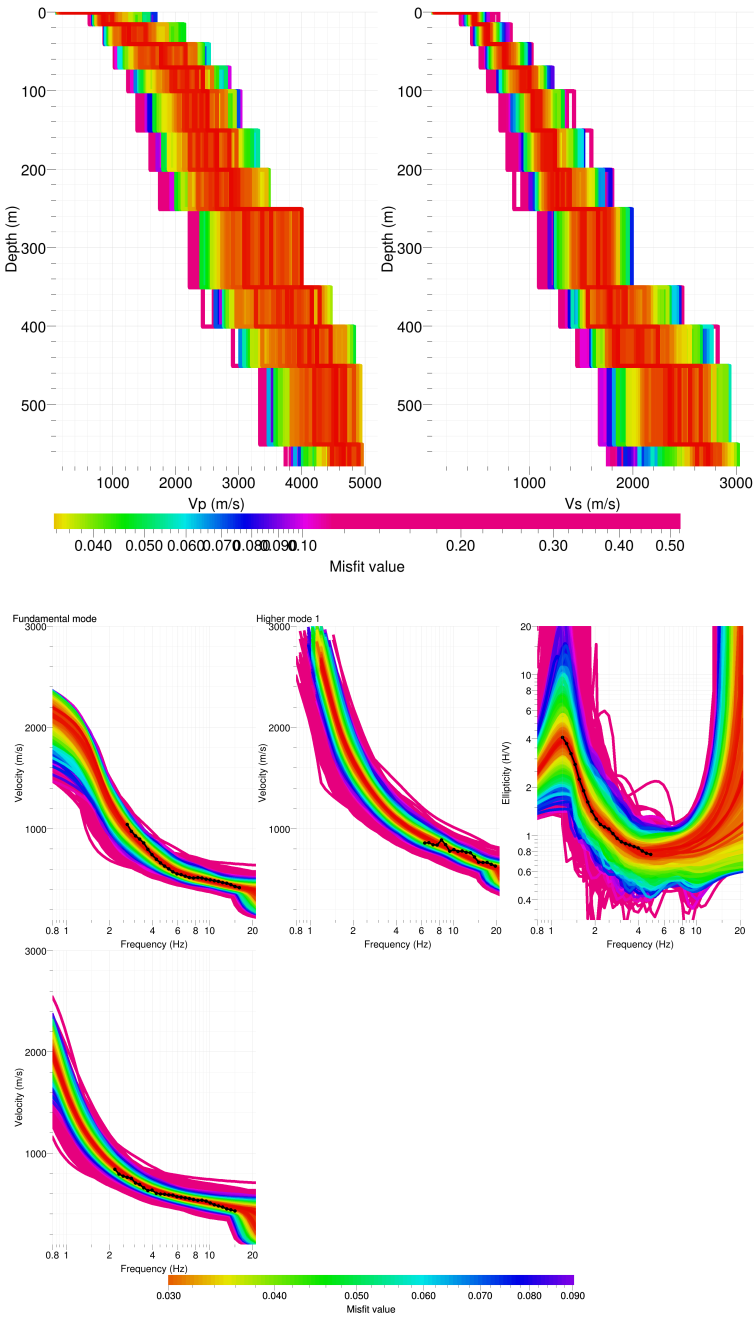

Figure 12: Inverted ground profiles in terms of V_p and V_s (top) and comparison between inverted models and measured Rayleigh and Love modes and corresponding ellipticity, fixed layer depth strategy.

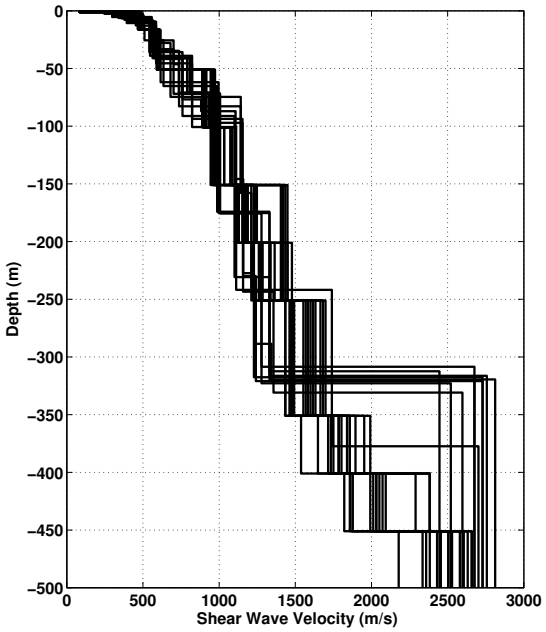

Figure 13: V_s ground profiles for the selected 25 best models.

6.2 Travel time average velocities and ground type

The distribution of the travel time average velocities at different depths was computed from the selected models. The uncertainty, computed as the standard deviation of the distribution of travel time average velocities for the considered models, is also provided, but its meaning is doubtful. $V_{s,30}$ is found to be $470\,\mathrm{m/s}$ corresponding to class B in the Eurocode 8 [CEN, 2004] and SIA261 [SIA, 2003].

	Mean (m/s)	**Uncertainty (m/s)**
$V_{s,5}$	297	66
$V_{s,10}$	359	41
$V_{s,20}$	427	33
$V_{s,30}$	469	25
$V_{s,40}$	497	25
$V_{s,50}$	524	26
$V_{s,100}$	655	13
$V_{s,150}$	750	17
$V_{s,200}$	828	13

Table 7: Travel time averages at different depths from the inverted models. Uncertainty is given as one standard deviation from the selected profiles.

6.3 SH transfer function and quarter-wavelength velocity

The quarter-wavelength velocity approach [Joyner et al., 1981] provides, for a given frequency, the average velocity at a depth corresponding to 1/4 of the wavelength of interest. It is useful to identify the frequency limits of the experimental data (minimum frequency in ellipticity, $1.2\,\mathrm{Hz}$ here, and dispersion curves, $2.2\,\mathrm{Hz}$ here). The results using this proxy show that no data is controlling the results below $170\,\mathrm{m}$, and the dispersion curves are controlling the results down to $60\,\mathrm{m}$ (Fig. 14). These results are probably under-estimating the depth where the method is sensitive. Moreover, the quarter wavelength impedance-contrast introduced by Poggi et al. [2012a] is also displayed in the figure. It corresponds to the ratio between two quarter-wavelength average velocities, respectively from the top and the bottom part of the velocity profile, at a given frequency [Poggi et al., 2012a]. It shows a trough (inverse shows a peak) at the resonance frequency.

Moreover, the theoretical SH-wave transfer function for vertical propagation [Roesset, 1970] is computed from the inverted profiles. It is compared to the quarter-wavelength amplification [Joyner et al., 1981], that however cannot take resonances into account (Fig. 15). In this case, the models are predicting an amplification up to a factor of 3 at the resonance frequencies. This will be compared to observations at this station.

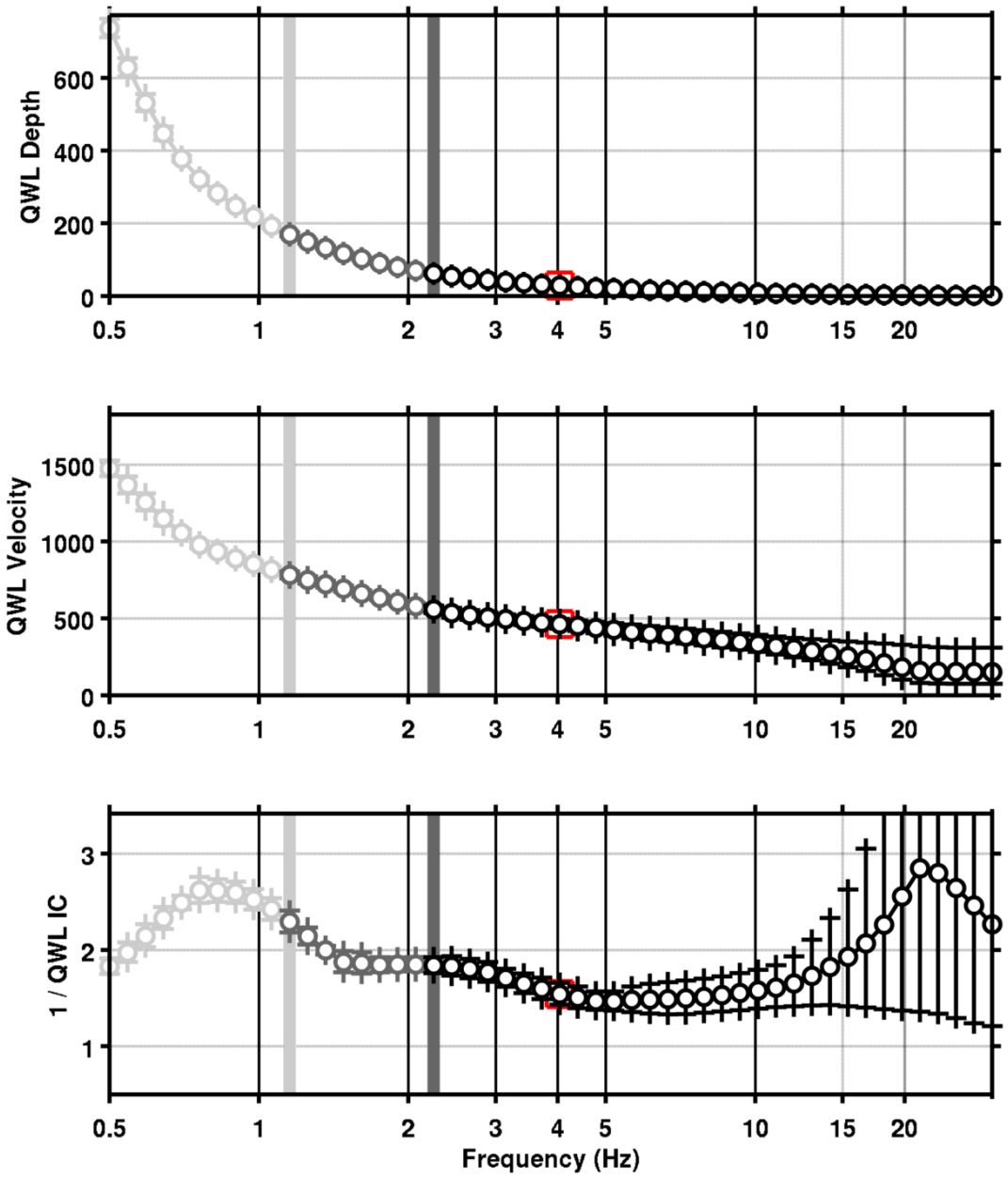

Figure 14: Quarter wavelength velocity representation of the velocity profile (top: depth, centre: velocity, bottom: inverse of the impedance contrast). Black curve is constrained by the dispersion curves, light grey is not constrained by the data. Red square is corresponding to $V_{s,30}$.

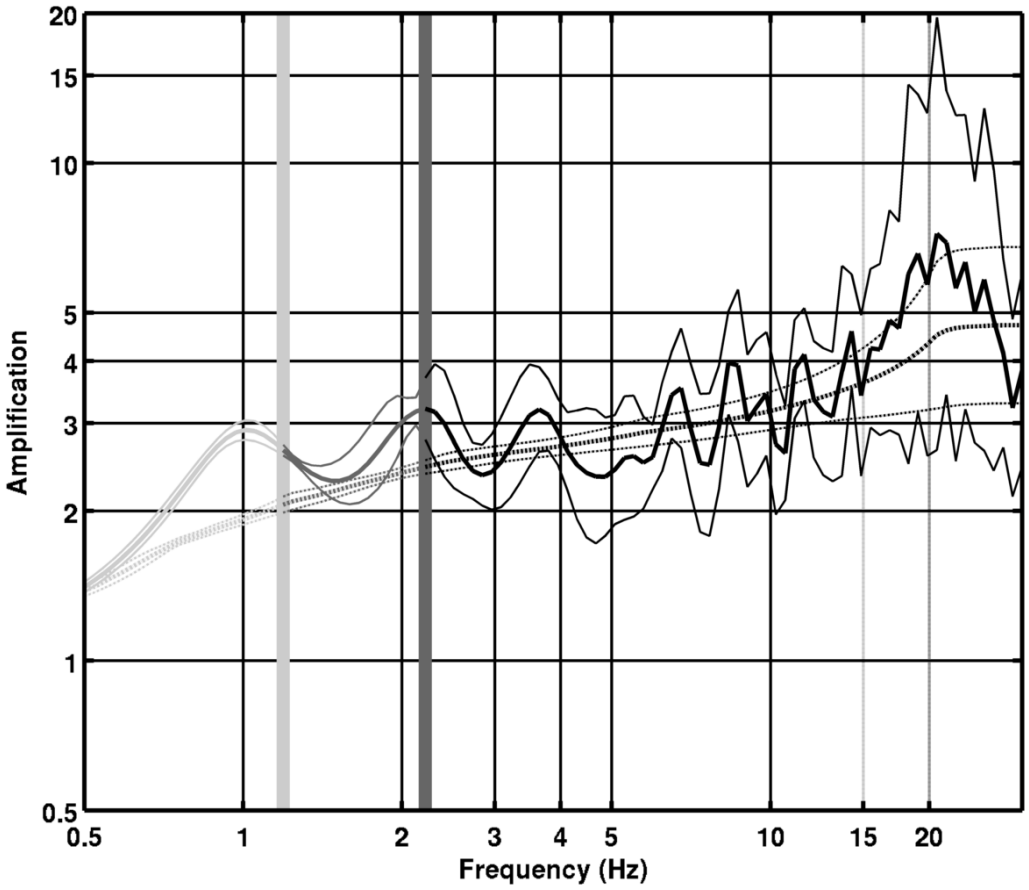

Figure 15: Theoretical SH transfer function (solid line) and quarter wavelength impedance contrast (dashed line) with their standard deviation. Significance of the greyshades is detailed in Fig. 14.

7 Conclusions

The array measurements performed in this study were successful in deriving a velocity model below the SALTS station. We found a gradient-type velocity profile from $300 - 400\,\mathrm{m/s}$ at the surface increasing up to $800\,\mathrm{m/s}$ between 50 and $90\,\mathrm{m}$ and up to $1500\,\mathrm{m/s}$ at $300\,\mathrm{m}$. The interface between sediment and bedrock is represented by a peak at $1.2\,\mathrm{Hz}$ in the ellipticity. This resonance may however be related to a 2D/3D behaviour of the alluvial fan. We derived a bedrock depth of $320\,\mathrm{m}$, which is consistent with geophysical and geomorpological data. The velocity in the bedrock is poorly constrained. $V_{s,30}$ is found to be close to $470\,\mathrm{m/s}$, which corresponds to ground type B in Eurocode 8 and SIA261 design codes. The theoretical SH transfer function and impedance contrast of the quarter-wavelength velocity computed from the inverted profiles show limited amplification at the resonance frequencies. Recordings on the new station will allow to validate these simple models.

Acknowledgements

The authors thank Ben Edwards for the help during the array measurements.

References

Sylvette Bonnefoy-Claudet, Fabrice Cotton, and Pierre-Yves Bard. The nature of noise wavefield and its applications for site effects studies. *Earth-Science Reviews*, 79(3-4): 205–227, December 2006. ISSN 00128252. doi: 10.1016/j.earscirev.2006.07.004. URL http://linkinghub.elsevier.com/retrieve/pii/S0012825206001012.

Janine Bühler. The earthquake of 1774 in the region of Altdorf, 2006.

Jan Burjánek, Gabriela Gassner-Stamm, Valerio Poggi, Jeffrey R. Moore, and Donat Fäh. Ambient vibration analysis of an unstable mountain slope. *Geophysical Journal International*, 180(2):820–828, February 2010. ISSN 0956540X. doi: 10.1111/j.1365-246X.2009.04451.x. URL http://doi.wiley.com/10.1111/j.1365-246X.2009.04451.x.

J. Capon. High-Resolution Frequency-Wavenumber Spectrum Analysis. *Proceedings of the IEEE*, 57(8):1408–1418, 1969.

CEN. *Eurocode 8: Design of structures for earthquake resistance - Part 1: General rules, seismic actions and rules for buildings*. European Committee for Standardization, en 1998-1: edition, 2004.

Donat Fäh, Fortunat Kind, and Domenico Giardini. A theoretical investigation of average H / V ratios. *Geophysical Journal International*, 145:535–549, 2001.

Donat Fäh, Gabriela Stamm, and Hans-Balder Havenith. Analysis of three-component ambient vibration array measurements. *Geophysical Journal International*, 172(1):199–213, January 2008. ISSN 0956540X. doi: 10.1111/j.1365-246X.2007.03625.x. URL http://doi.wiley.com/10.1111/j.1365-246X.2007.03625.x.

Donat Fäh, Marc Wathelet, Miriam Kristekova, Hans-Balder Havenith, Brigitte Endrun, Gabriela Stamm, Valerio Poggi, Jan Burjanek, and Cécile Cornou. Using Ellipticity Information for Site Characterisation Using Ellipticity Information for Site Characterisation. Technical report, NERIES JRA4 Task B2, 2009.

Stefan Fritsche. *Large Historical Earthquakes in Switzerland Multidisciplinary Studies on Damage Fields and Site-Effects*. PhD thesis, ETH Zurich, 2008.

William B. Joyner, Richard E. Warrick, and Thomas E. Fumal. The effect of Quaternary alluvium on strong ground motion in the Coyote Lake, California, earthquake of 1979. *Bulletin of the Seismological Society of America*, 71(4):1333–1349, 1981.

Katsuaki Konno and Tatsuo Ohmachi. Ground-Motion Characteristics Estimated from Spectral Ratio between Horizontal and Vertical Components of Microtremor. *Bulletin of the Seismological Society of America*, 88(1):228–241, 1998.

Frank O. Nitsche, Alan G. Green, Heinrich Horstmeyer, and Frank Büker. Late Quaternary depositional history of the Reuss delta, Switzerland: constraints from high-resolution seismic reflection and georadar surveys. *Journal of Quaternary Science*, 17(2):131–143, February 2002. ISSN 0267-8179. doi: 10.1002/jqs.645. URL http://doi.wiley.com/10.1002/jqs.645.

Valerio Poggi and Donat Fäh. Estimating Rayleigh wave particle motion from three-component array analysis of ambient vibrations. *Geophysical Journal International*, 180(1):251–267, January 2010. ISSN 0956540X. doi: 10.1111/j.1365-246X.2009.04402.x. URL http://doi.wiley.com/10.1111/j.1365-246X.2009.04402.x.

Valerio Poggi, Benjamin Edwards, and D. Fah. Characterizing the Vertical-to-Horizontal Ratio of Ground Motion at Soft-Sediment Sites. *Bulletin of the Seismological Society of America*, 102(6):2741–2756, December 2012a. ISSN 0037-1106. doi: 10.1785/0120120039. URL http://www.bssaonline.org/cgi/doi/10.1785/0120120039.

Valerio Poggi, Donat Fäh, Jan Burjanek, and Domenico Giardini. The use of Rayleigh-wave ellipticity for site-specific hazard assessment and microzonation: application to the city of Lucerne, Switzerland. *Geophysical Journal International*, 188(3):1154–1172, March 2012b. ISSN 0956540X. doi: 10.1111/j.1365-246X.2011.05305.x. URL http://doi.wiley.com/10.1111/j.1365-246X.2011.05305.x.

J.M. Roesset. Fundamentals of soil amplification. In R. J. Hansen, editor, *Seismic Design for Nuclear Power Plants*, pages 183–244. M.I.T. Press, Cambridge, Mass., 1970. ISBN 978-0-262-08041-5. URL http://mitpress.mit.edu/catalog/item/default.asp?ttype=2\&tid=5998.

SIA. *SIA 261 Actions sur les structures porteuses*. Société suisse des ingénieurs et des architectes, Zürich, sia 261:20 edition, 2003.

Marc Wathelet. An improved neighborhood algorithm: Parameter conditions and dynamic scaling. *Geophysical Research Letters*, 35(9):1–5, May 2008. ISSN 0094-8276. doi: 10.1029/2008GL033256. URL http://www.agu.org/pubs/crossref/2008/2008GL033256.shtml.